



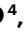






Acousto-optic modulation of gigawatt-scale laser pulses in ambient air

Received: 16 May 2023

Accepted: 7 September 2023

Published online: 02 October 2023

 Check for updates

Yannick Schrödel ^{1,2,3}✉, Claas Hartmann⁴, Jiaan Zheng¹, Tino Lang¹, Max Steudel⁵, Matthias Rutsch⁴, Sarper H. Salman ^{1,2,3}, Martin Kellert⁶, Mikhail Pergament⁶, Thomas Hahn-Jose⁷, Sven Suppelt ⁴, Jan Helge Dörsam ⁴, Anne Harth ⁵, Wim P. Leemans^{1,8}, Franz X. Kärtner ^{6,8,9}, Ingmar Hartl ¹, Mario Kupnik ⁴ & Christoph M. Heyl ^{1,2,3}✉

Control over the intensity, shape, direction and phase of coherent light is essential in numerous fields, from gravitational wave astronomy, quantum metrology and ultrafast sciences to semiconductor fabrication. Modern photonics, however, can involve parameter regimes where the wavelength or high optical powers involved restrict control due to absorption, light-induced damage or optical nonlinearity in solid media. Here we propose to circumvent these constraints using gaseous media tailored by high-intensity ultrasound waves. We demonstrate an implementation of this approach by efficiently deflecting ultrashort laser pulses using ultrasound waves in ambient air, without the use of transmissive solid media. At optical peak powers of 20 GW, exceeding previous limits of solid-based acousto-optic modulation by about three orders of magnitude, we reach a deflection efficiency greater than 50% while preserving excellent beam quality. Our approach is not limited to laser pulse deflection; gas-phase photonic schemes controlled by sonic waves could potentially be useful for realizing a new class of optical elements such as lenses or waveguides, which are effectively invulnerable against damage and can operate in new spectral regions.

The main underlying parameter governing the propagation of light in a medium is the medium's refractive index, n . Tailoring n represents an important foundation for many photonic control schemes^{1–5}. When an optical wave propagates through a medium, its phase velocity changes from c_0 , the speed of light in vacuum, to c_0/n . This ultimately leads to a change in phase and intensity. For example, an interface between different refractive indices causes a change in propagation direction of light both in reflection and transmission¹. The strength of this effect depends on the difference between the refractive indices Δn and the incident angle⁶. Large refractive index differences on the order of

$\Delta n \approx 0.5$ can be reached at the boundary between gases and transparent solids for most optical wavelengths⁷. This is a key reason why bulk media are used almost exclusively for optical elements such as lenses, mirrors, waveguides, among many others.

However, with the rapid progress in high-peak-power laser technology⁸ and applications^{9–11} reaching into novel wavelength regimes^{12,13}, established solid-based control schemes face severe limitations. Compared to gases, glasses are transmissive only in a relatively small spectral range; they restrict the optical peak and average power through light-induced damage¹⁴, as well as thermal lensing¹⁵, and cause

¹Deutsches Elektronen-Synchrotron DESY, Hamburg, Germany. ²Helmholtz Institute Jena, Jena, Germany. ³GSI Helmholtzzentrum für Schwerionenforschung GmbH, Darmstadt, Germany. ⁴Measurement and Sensor Technology Group, Technische Universität Darmstadt, Darmstadt, Germany. ⁵Center of Optical Technologies, Aalen University, Aalen, Germany. ⁶Center for Free-Electron Laser Science CFEL, Deutsches Elektronen-Synchrotron DESY, Hamburg, Germany. ⁷Inoson GmbH, St. Ingbert, Germany. ⁸Department of Physics, University of Hamburg, Hamburg, Germany. ⁹The Hamburg Centre for Ultrafast Imaging, Hamburg, Germany. ✉e-mail: yannick.schroedel@desy.de; christoph.heyhl@desy.de

losses at boundary layers. For intense or ultrashort pulses, additional restrictions arise due to dispersion and nonlinear optical effects such as self-focusing¹⁶. One powerful route to circumvent some of these limitations has been opened by meta-optics^{17,18}, relying on nanostructured dielectric media.

An entirely different route is the employment of gaseous photonic media. In contrast to solids, gases are immune to damage and support about three orders of magnitude higher peak powers at very little dispersion within large spectral regions. Their refractive index, however, is very close to 1, limiting Δn for gas-based photonic systems. In addition, creating a static refractive index boundary in gases poses a technical challenge. However, in the limit of small incident angle (grazing incidence), light reflection can still occur even for small Δn . In nature, this phenomenon is well known: in a mirage, layers of air at different temperature levels, with Δn on the order of only 10^{-5} , can substantially alter the optical path⁷. Applying similar principles, gas-phase refractive elements² such as lenses¹⁹, beam samplers²⁰ and intracavity acousto-optic (AO) loss modulators²¹, as well as gratings using multiple plasma layers²², have been developed.

Strikingly, more advanced gas-based schemes enabling superior control options including efficient acousto-optic modulation (AOM) have not yet entered the photonics field. In this Article, we demonstrate a novel light control method employing highly intense ultrasound waves in air. To achieve this, we engineer a transmissive optical Bragg grating by periodic sinusoidal pressure modulation²³ using high-pressure ultrasound, enabling efficient AOM in ambient air.

Acousto-optics, from solids to gases

The field of acousto-optics describes the interaction between optic and acoustic waves. Upon interaction of the two waves, quantized as a photon and a phonon, they can scatter²⁴. Momentum and energy conservation lead to partial redirection and a frequency shift. This enables direct control over the optical frequency, propagation direction, phase and intensity through the AO effect via the readily accessible acoustic frequency F (100-MHz range for solid media) and the acoustic power. The acoustic wavelength λ appears as a periodic modulation of the optical refractive index with a magnitude on the order of $\lambda = V/F \approx 10 \mu\text{m}$, where V is the speed of sound. When the refractive index modulation depth $\Delta n(x, t)$ is sufficiently high and the interaction length L is large enough²⁵, optimal conversion into the first diffraction order $m = +1$ can be achieved by phase-matching of the diffracted and incident ($m = 0$) waves. This interaction type is called the Bragg regime, where scattering into higher diffraction orders is minimized. Bragg diffraction is the most commonly used diffraction regime for AO modulators and deflectors²⁵ as opposed to the Raman–Nath regime, where higher orders are typically present²⁶. The Klein–Cook parameter (Q)²⁴

$$Q = \frac{2\pi\lambda LF^2}{nV^2 \cos \theta} \quad (1)$$

quantifies the diffraction regimes, with $Q \ll 1$ defining Raman–Nath diffraction and $Q \gg 1$ (typically used $Q \geq 7$) Bragg diffraction^{24,25}. Here, θ is the incident angle, n denotes the average refractive index and λ is the optical wavelength.

In the Bragg regime, conversion is reached when the angle θ between incident beam propagation direction and the acoustic wavefronts fulfils the Bragg condition

$$\sin \theta_B = \frac{\lambda F}{2V} \quad (2)$$

Diffraction efficiencies into the ($m = +1$) order of close to 100% have been achieved in solid-state AO modulators, and these are widespread in modern photonics. Applications include active Q-switching and cavity dumping by loss modulation²⁷, stabilization

of the carrier-envelope phase²⁸ and optical gating²⁹. Employed as AO tunable filters³⁰ and as programmable dispersive filters^{31,32}, AO devices have been used to spectrally select and shape the phase of ultrashort pulses. The AO medium used to carry the acoustic wave determines the characteristics of the AOM. A number of crystalline^{33–36} and liquid^{37–39} materials have been used, with TeO_2 and crystalline germanium being the most common. Other works demonstrated the AO effect for similar applications such as mode locking or lensing in liquid media^{40–42}, with limitations very similar to bulk-based AOM.

Employment of a gas as the AO medium has so far only been reported with low diffraction efficiencies: for the far infrared using a high-pressure gas vessel⁴³, in the mid-infrared to modulate intracavity losses for He–Ne and Ar-ion lasers in cylindrical configurations²¹, and as a beam sampler²⁰, demonstrating the AO effect using ambient air as the AO medium. Here, however, the diffraction efficiencies were very small, and in the case of ref. 21, no diffracted beam could be separated or characterized. This can be attributed to the acoustic properties of gases setting severe technical challenges: the first one is the low Δn in gases, arising from the pressure modulation Δp and the emerging temperature differences with $\Delta n \approx \Delta p \times (n - 1)$. Even for high sound pressure levels (SPLs) of, for example, 140 dB, Δn in air reaches values on the order of only 10^{-7} . The second challenge is the high ultrasound field absorbance for even comparatively low F , effectively limiting the acoustic frequencies to values below a few megahertz⁴⁴. To ensure efficient AOM in gases, two requirements must be met. First, to ensure strong scattering²⁴, Δn must be large enough, and a shallow incidence angle must be used to take advantage of high Fresnel reflectance at grazing incidence. Separability of the diffracted and transmitted beams sets a lower bound on the incidence angle and thus on F . For example, a Gaussian beam with a $1/e^2$ -radius of $w_0 = 3.5 \text{ mm}$ in the NIR ($\lambda = 1 \mu\text{m}$) has a diffraction-limited beam divergence of $\theta_0 \approx 100 \mu\text{rad}$. Using equation (2), we determine that a beam deflection angle of $2\theta_B \geq 4\theta_0$ requires $F \geq 135 \text{ kHz}$ for AOM in air. Second, the transducer length L must be optimized with respect to Δn and the angular acceptance^{25,45,46}. Although a small Δn demands a large AO interaction length, the angular acceptance shrinks with growing L . Figure 1a illustrates the principle of AOM employing a shallow angle in air, where spatial separation of transmitted and deflected beams is enabled in the far field.

Results

Basic characteristics of gas-phase AOM

Our experimental demonstrations of gas-based AO are carried out in ambient air using ultrashort laser pulses centred at 1,030 nm. Figure 2a shows a schematic of the experimental set-up, which employs all-reflective bulk optical elements. An incident laser beam passes seven times across an ultrasound field volume with a diameter of 7 cm to increase the interaction length while keeping the ultrasound transducer at a reasonable size. The employed multi-pass scheme effectively increases L . A side effect is an acoustic phase added every pass due to an acquired vertical shift of the laser beam. This acoustic phase can influence the diffraction and must be considered for set-up optimization. An ultrasound transducer generates the ultrasound field and an optional planar reflector mounted to reflect the acoustic waves enhances the SPL by creating a standing ultrasound wave. After AO interaction, the laser beams are routed to diagnostics, enabling characterization of the beam quality and power in all diffraction orders. The transducer operates at $F = 490 \text{ kHz}$, yielding an acoustic wavelength of $\lambda = 700 \mu\text{m}$. This leads to illumination of approximately ten acoustic wavelengths, as shown in Fig. 1c. The Klein–Cook parameter for this geometry is $Q = 6.5$ according to equation (1), placing the interaction geometry approximately into the Bragg regime.

The light source for our first experimental demonstration is a fibre-coupled mode-locked laser delivering ultrashort pulses ($\sim 150 \text{ fs}$) at a pulse repetition rate of 54 MHz. For this experiment, we used an average output power of a few tens of milliwatts, preventing

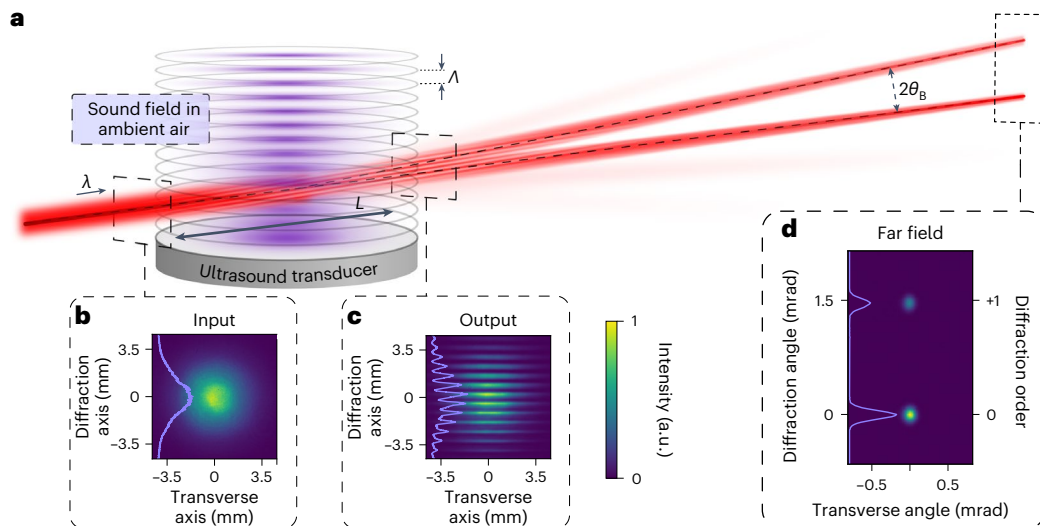


Fig. 1 | Schematic of ultrasound-assisted angular deflection of a laser beam in air. **a**, A laser beam (red) in a gaseous medium entering a sound field at a shallow Bragg angle relative to the sound field wavefronts (purple). Bragg-type AOM leads to efficient deflection of the incident beam at twice the Bragg angle and at higher diffraction orders carrying minimal energy. **b–d**, Camera-measured

beam profiles and corresponding centred lineouts along the diffraction axis of an approximately Gaussian-shaped incident beam (**b**), directly after the AO interaction, exhibiting interference-induced fringes (**c**), and in the far field (**d**). The data were recorded in a multi-pass set-up that enabled an increased interaction length.

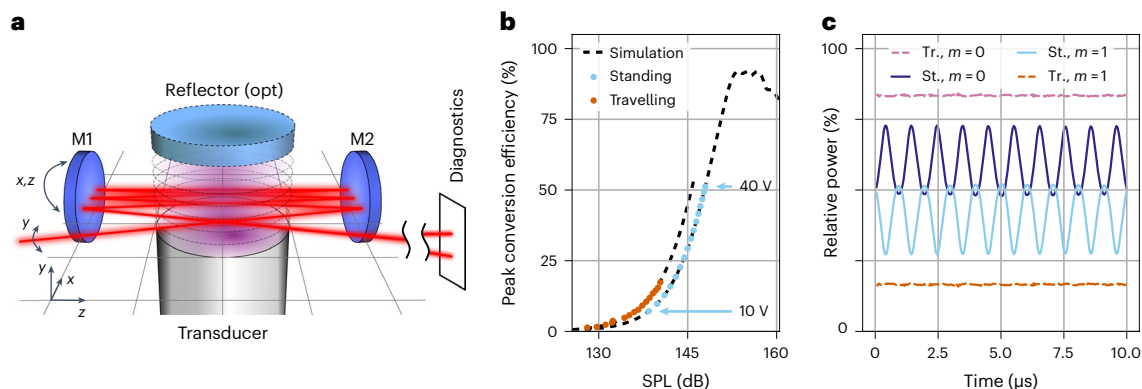


Fig. 2 | Experimental set-up and dependence of the deflection efficiency on acoustic power and time. **a**, Schematic of the AO interaction geometry. Mirrors M1 and M2 of the multi-pass folding geometry are indicated in blue. The resulting beam path is marked red. The optional acoustic reflector is shown in light blue. **b**, Maximum achieved conversion efficiency into the first diffraction order ($m = +1$) as a function of SPL for both the standing acoustic wave (blue dots) and

travelling acoustic wave without the optional reflector (orange dots), displayed together with the simulated signals (black dashed line). Standing acoustic wave data points are fitted to simulated data. The applied driver supply voltage boundaries are indicated. **c**, Time evolution of the relative powers of diffracted ($m = +1$) and transmitted ($m = 0$) orders of both standing (St., light/dark blue lines) and travelling (Tr., orange/purple dashed lines) wave configurations.

any nonlinear effects. Beam delivery via a polarization-maintaining single-mode fibre ensures an excellent spatial beam quality (Fig. 1b), corresponding to a beam-quality factor of $M^2 = 1.04$ in both axes. The collimated beam is subsequently sent into the ultrasound field at $\theta_B \approx 0.75$ mrad relative to the sound wavefronts. Following the AO interaction, the output beam exhibits interference fringes caused by the interference of all transmitted diffraction orders (Fig. 1c). In the far field (Fig. 1d), the diffraction orders are separated by $2\theta_B \approx 1.5$ mrad, an angle almost an order of magnitude larger than the beam divergence. Transmitted and diffracted beams display an M^2 of 1.15 in both axes for both beams ($m = 0, m = +1$), demonstrating that an excellent beam quality is maintained upon AO interaction.

Figure 2b displays the measured diffraction efficiency, defined as the ratio of the optical power in the first ($m = +1$) order and the input optical power, as a function of SPL for two configurations—with (red) and without (blue) acoustic reflector. In addition, the numerically

calculated efficiency is displayed for both configurations. The simulations employ finite-element methods (FEMs) for two-dimensional (2D) acoustics simulation, and nonlinear split-step Fourier methods for 2 + 1-dimensional optical beam propagation (Methods). The sound field simulations are based on transducer surface velocity data extracted via laser-Doppler vibrometry. We adjust the ultrasound field strength by scanning the supply voltage of the driver of the ultrasound transducer. The voltage is tied to the transducer's surface velocity and therefore to the induced SPL. The SPL is difficult to determine as acoustic microphones typically impact the sound field, particularly for a standing-wave configuration. We therefore choose to calibrate the SPL for the standing-wave case by fitting the measured data points to the simulated efficiency curves. For the travelling-wave configuration, we use a commercial optical microphone to calibrate the SPL. The efficiency trace displayed in Fig. 2b (orange dots) shows excellent agreement with the numerical simulations (dashed line).

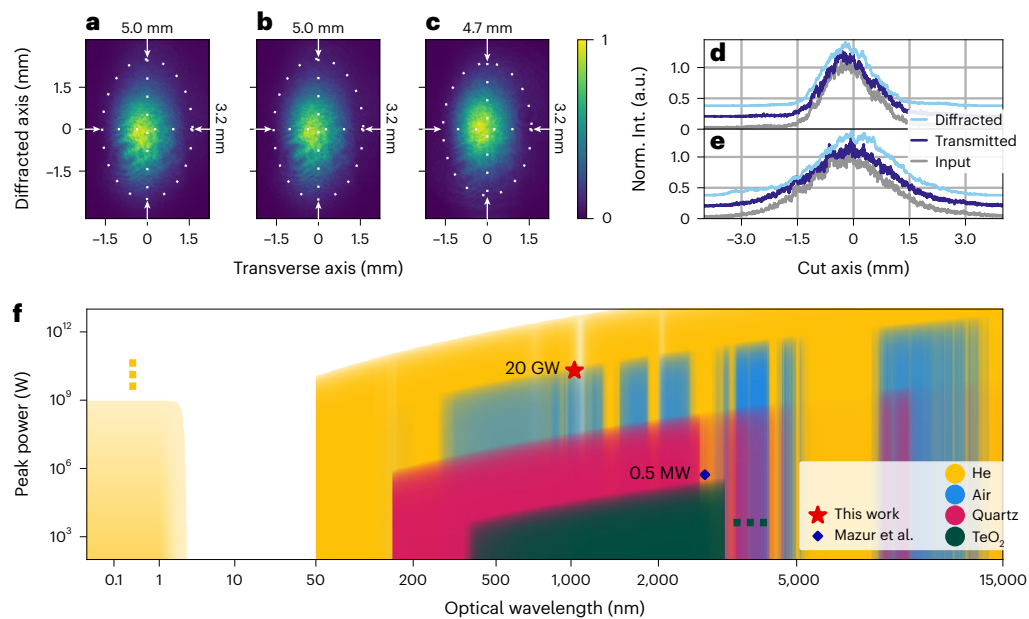


Fig. 3 | AO diffraction of ultrashort laser pulses at high peak power.

a–c. Measured spatial profiles of the input (**a**), transmitted (**b**) and diffracted (**c**) beams. The major and minor axes, the $1/e^2$ diameters and the circumferences of fitted elliptical Gaussian beams are annotated (white dashes and arrows). **d,e.** Centred lineouts along the transverse (**d**) and diffracted (**e**) axes are shown, normalized and vertically offset to improve readability. **f.** Possible parameter

regimes of gas (yellow, helium; blue, air) and bulk-based (purple, quartz/fused silica; green, TeO₂) AO media, limited by critical power and linear absorption, displayed together with the here-reported result (red star). Areas where data were not available are indicated using dotted line markers. Blue diamond: ref. 49, using a KG(WO₄)₂ crystal as the AO medium. For data sources and details see Methods.

The simulations indicate that the travelling-wave configuration exhibits a slightly higher diffraction efficiency within the explored SPL range. This effect may be explained by a more homogeneous sound field for the travelling-wave case and/or inaccuracies in the numerical model for the resonant acoustic wave. The maximum efficiency is obtained using the acoustic reflector, yielding a diffraction efficiency into the first order exceeding 50%. In comparison, the travelling wave without reflector can only deflect up to 20% of the incident power. Strikingly, the numerical simulation indicates much higher diffraction efficiencies with further increased SPLs.

The two configurations, employing both travelling and standing waves, exhibit a vastly different temporal behaviour. The temporal characteristics were measured using photodiodes and are shown in Fig. 2c, corresponding to the data points obtained at maximum voltage displayed in Fig. 2b. The travelling-wave case displays a constant relative optical power for both diffraction orders. In contrast, the configuration using an acoustic resonator modulates the laser beams, reflecting the temporal amplitude oscillation of a standing wave with a modulation frequency equal to $2F \approx 1$ MHz, entering the megahertz range. Although a perfect standing wave expectedly exhibits periodic instants in time where the ultrasound field vanishes completely, we observe that the diffracted beam does not completely vanish. We attribute this to the acoustic field not exhibiting exclusively a fundamental transverse mode but showing phase variations across the radial extent of the ultrasound resonator.

Although resonant AOM enables modulation and switching of optical signals at $2F$, non-resonant (travelling wave) AOM offers more versatile temporal modulation options at reduced rates. Both the speed of sound V and the beam diameter, as well as the transducer's response, define the AO rise time, which determines these rates. In our experiment, we determine the 10% to 90% rise time for non-resonant AOM to be 32 μ s (Methods), corresponding to a possible modulation frequency in the 100-kHz range. This may be improved by reducing the transducer rise time and/or employing gases with higher V .

Gigawatt-scale AOM

In a second experiment using the same optical set-up, we employ ultrashort (760 fs) pulses with a pulse energy of up to 15.2 mJ and a corresponding peak power of up to 20 GW, delivered by a high-power laser amplifier⁴⁷. The laser operates in burst mode (Methods) with an intra-burst average power of 3.5 kW. Figure 3a presents a camera image of the transmitted beam where no AO interaction has occurred (ultrasound transducer off), that is, the laser beam simply propagates through the set-up using the guiding mirrors. Figure 3b shows the transmitted beam profile with the active transducer. Finally, Fig. 3c shows the spatially separated diffracted order at a diffraction efficiency of ~25%. The ultrasound transducer was operated at a lower SPL compared to the maximum values shown in Fig. 2b, limited by the driving electronics hardware available at the time of the experiment. The measured efficiencies match those obtained using the fibre-coupled light source. In this experiment, the diffracted and transmitted orders are spatially separated by 16.5-m beam propagation of a low-power fraction of the output beam behind the AO interaction and measured via a lens telescope and a camera. Figure 3d,e shows centred lineouts of the beam profiles along the transverse (Fig. 3d) and diffraction (Fig. 3e) axes, respectively. The very similar beam shapes and sizes indicate preservation of the beam quality.

The peak power is limited by the onset of self-focusing, expected when exceeding the critical power of air (~5–10 GW)⁴⁸. We observed this onset in our experiments at a maximum peak power of 20 GW as a slightly reduced beam diameter following ~4 m of beam propagation. Figure 3f presents the parameters peak power and optical wavelength used in our experiment (red star), together with estimated parameter regimes supporting AOM in helium (yellow shading) and air (blue shading). The commonly used bulk AOM materials quartz/fused silica (purple shading) and TeO₂ (green shading) are shown for comparison, along with reported values of a record peak power obtained using bulk AOM⁴⁹ employing KG(WO₄)₂ (crystals; blue diamond). The critical power and linear absorption define the displayed limits (Methods).

Possible limitations arising due to geometrical restrictions such as a minimum diffraction angle supporting beam separation are not taken into account. The figure clearly shows the superior peak power performance of the demonstrated gas AOM, exceeding earlier records by more than three orders of magnitude⁵⁰. In addition, the figure indicates the potential to extend gas-based photonic devices such as AOM technology into the ultraviolet and beyond, as well as into the mid-infrared.

Conclusion and outlook

In this Article, we have demonstrated efficient and beam quality-preserving deflection of gigawatt-scale laser pulses via AOM in ambient air while entirely omitting transmissive bulk optics. Our results demonstrate a major peak power boost for AOM, limited by the critical power of the gas-phase AO medium. Considering lighter gases and/or gas media at reduced pressure, gas-phase AOM can prospectively be scaled further, approaching the terawatt regime. Contrarily, the use of heavier gases with larger refractive indices and/or higher gas densities may enable diffraction efficiencies dramatically exceeding 50%. Alternatively, more advanced ultrasound transducer schemes targeting increased SPL could enable an efficiency boost, as indicated by our numerical simulations. In addition, using gases as AO media opens a route towards AOM in new spectral regions—ambient air is transmissive in ranges from ~250 nm towards the NIR and mid-infrared, thus exceeding the transmission band of solids dramatically. Noble gases such as helium can prospectively support an even wider spectral range, including the ultraviolet region down to ~50 nm and the transparent window for photon energies above 1 keV.

Gas-phase AOM can thus be expected to open entirely new parameter regimes for AOM technology, with great prospects for applications such as optical switches and pulse pickers, beamsplitters and combiners, phase modulators, spectral filters, dispersion control and many more. This means that the limited acoustic modulation frequency has to be taken into account. Moreover, the concept of employing gas-phase media tailored via intense ultrasound waves can be further expanded beyond AOM, opening the door to versatile gas-based photonics. This may include lenses, waveguides, optical gratings and considerably more, translating photonic devices from solid-state media to the gas phase, thereby opening a new field—gas-phase sono-photonics.

Online content

Any methods, additional references, Nature Portfolio reporting summaries, source data, extended data, supplementary information, acknowledgements, peer review information; details of author contributions and competing interests; and statements of data and code availability are available at <https://doi.org/10.1038/s41566-023-01304-y>.

References

1. Yu, N. et al. Light propagation with phase discontinuities: generalized laws of reflection and refraction. *Science* **334**, 333–337 (2011).
2. Drescher, L. et al. Extreme-ultraviolet refractive optics. *Nature* **564**, 91–94 (2018).
3. Tirole, R. et al. Double-slit time diffraction at optical frequencies. *Nat. Phys.* **19**, 999–1002 (2023).
4. Balla, P. et al. Ultrafast serrodyne optical frequency translator. *Nat. Photon.* **17**, 187–192 (2023).
5. Berti, N., Coen, S., Erkintalo, M. & Fatome, J. Extreme waveform compression with a nonlinear temporal focusing mirror. *Nat. Photon.* **16**, 822–827 (2022).
6. Fresnel, A. Note sur le calcul des teintes que la polarisation développe dans les lames cristallisées. *Ann. Chim. Phys.* **17**, 101–112 (1821).
7. Ciddor, P. E. Refractive index of air: new equations for the visible and near infrared. *Appl. Opt.* **35**, 1566–1573 (1996).
8. Mourou, G. Nobel lecture: Extreme light physics and application. *Rev. Mod. Phys.* **91**, 030501 (2019).
9. Albert, F. et al. 2020 roadmap on plasma accelerators. *New J. Phys.* **23**, 031101 (2021).
10. Biegert, J., Calegari, F., Dudovich, N., Quéré, F. & Vrakking, M. Attosecond technology(ies) and science. *J. Phys. B At. Mol. Opt. Phys.* **54**, 070201 (2021).
11. Kodama, R. et al. Fast heating scalable to laser fusion ignition. *Nature* **418**, 933–934 (2002).
12. Lindroth, E. et al. Challenges and opportunities in attosecond and XFEL science. *Nat. Rev. Phys.* **1**, 107–111 (2019).
13. Maroju, P. K. et al. Attosecond pulse shaping using a seeded free-electron laser. *Nature* **578**, 386–391 (2020).
14. Natoli, J.-Y., Gallais, L., Akhouayri, H. & Amra, C. Laser-induced damage of materials in bulk, thin-film and liquid forms. *Appl. Opt.* **41**, 3156–3166 (2002).
15. Gordon, J. P. et al. Long-transient effects in lasers with inserted liquid samples. *J. Appl. Phys.* **36**, 3–8 (1965).
16. Kelley, P. L. Self-focusing of optical beams. *Phys. Rev. Lett.* **15**, 1005–1008 (1965).
17. Kamali, S. M. et al. A review of dielectric optical metasurfaces for wavefront control. *Nanophotonics* **7**, 1041–1068 (2018).
18. Ossiander, M. et al. Extreme ultraviolet metalens by vacuum guiding. *Science* **380**, 59–63 (2023).
19. Michaelis, M. M. et al. A gas-lens telescope. *Nature* **353**, 547–548 (1991).
20. Vandamme, E. & Muys, P. Ultrasonic beamsplitter for high-power CO₂ lasers. *J. Opt. A Pure Appl. Opt.* **3**, S68 (2001).
21. Grulkowski, I., Jankowski, D. & Kwiek, P. Acousto-optic interaction with the use of cylindrical ultrasonic waves in the laser cavity. *Appl. Opt.* **48**, C81 (2009).
22. Michine, Y. & Yoneda, H. Ultra high damage threshold optics for high power lasers. *Commun. Phys.* **3**, 24 (2020).
23. Phariseau, P. On the diffraction of light by progressive supersonic waves: oblique incidence: intensities in the neighbourhood of the Bragg angle. *Proc. Ind. Acad. Sci. A* **44**, 165–170 (1956).
24. Klein, W. R. & Cook, B. D. Unified approach to ultrasonic light diffraction. *IEEE Trans. Sonics Ultrasonics* **14**, 123–134 (1967).
25. Goutzoulis, A. P., Pape, D. R. & Kulakov, S. V. (eds) *Design and Fabrication of Acousto-Optic Devices*. Vol. 41 Optical Engineering (Marcel Dekker, 1994).
26. Baryshev, V. N. & Epikhin, V. M. Compact acousto-optic modulator operating in the purely Raman-Nath diffraction regime as a phase modulator in FM spectroscopy. *Quantum Electron.* **40**, 431 (2010).
27. Plaessmann, H., Yamada, K. S., Rich, C. E. & Grossman, W. M. Subnanosecond pulse generation from diode-pumped acousto-optically Q-switched solid-state lasers. *Appl. Opt.* **32**, 6616 (1993).
28. Jones, D. J. et al. Carrier-envelope phase control of femtosecond mode-locked lasers and direct optical frequency synthesis. *Science* **288**, 635–639 (2000).
29. Schwenger, W. J. & Higbie, J. M. High-speed acousto-optic shutter with no optical frequency shift. *Rev. Sci. Instrum.* **83**, 083110 (2012).
30. Harris, S. E. & Wallace, R. W. Acousto-optic tunable filter. *J. Opt. Soc. Am.* **59**, 744–747 (1969).
31. Tournois, P. Acousto-optic programmable dispersive filter for adaptive compensation of group delay time dispersion in laser systems. *Opt. Commun.* **140**, 245–249 (1997).
32. Shim, S.-H., Strasfeld, D. B., Fulmer, E. C. & Zanni, M. T. Femtosecond pulse shaping directly in the mid-IR using acousto-optic modulation. *Opt. Lett.* **31**, 838–840 (2006).
33. Yano, T., Fukumoto, A. & Watanabe, A. Tellurite glass: a new acousto-optic material. *J. Appl. Phys.* **42**, 3674–3676 (1971).
34. Abrams, R. L. & Pinnow, D. A. Acousto-optic properties of crystalline germanium. *J. Appl. Phys.* **41**, 2765–2768 (1970).
35. Pinnow, D. A., Van Uitert, L. G., Warner, A. W. & Bonner, W. A. Lead molybdate: a melt-grown crystal with a high figure of merit for acousto-optic device applications. *Appl. Phys. Lett.* **15**, 83–86 (1969).

36. Krause, J. T., Kurkjian, C. R., Pinnow, D. A. & Sigety, E. A. Low acoustic loss chalcogenide glasses—a new category of materials for acoustic and acousto-optic applications. *Appl. Phys. Lett.* **17**, 367–368 (1970).
37. Nagai, S., Peters, A. & Candau, S. Acousto-optical effects in a nematic liquid crystal. *Rev. Phys. Appl.* **12**, 21–30 (1977).
38. Nikitin, P. A., Voloshinov, V. B., Gerasimov, V. V. & Knyazev, B. A. Acousto-optic modulation and deflection of terahertz electromagnetic radiation in nonpolar liquids. *Tech. Phys. Lett.* **43**, 635–637 (2017).
39. Szulzycki, K., Savaryn, V. & Grulkowski, I. Generation of dynamic Bessel beams and dynamic bottle beams using acousto-optic effect. *Opt. Exp.* **24**, 23977 (2016).
40. Ferria, K., Grulkowski, I. & Kwiek, P. Acousto-optic lens based on interaction of narrow laser beam with cylindrical ultrasound. *J. Phys. IV France* **137**, 67–72 (2006).
41. Grulkowski, I., Jankowski, D. & Kwiek, P. Acousto-optic interaction of a Gaussian laser beam with an ultrasonic wave of cylindrical symmetry. *Appl. Opt.* **46**, 5870–5876 (2007).
42. Kwiek, P. Mode locking of argon ion laser by use of cylindrical ultrasonic waves. *Opt. Commun.* **283**, 2224–2227 (2010).
43. Dürr, W. Acousto-optic interaction in gases and liquid bases in the far infrared. *Int. J. Infrared Millimeter Waves* **7**, 1537–1558 (1986).
44. Bond, L. J., Chiang, C.-H. & Fortunko, C. M. Absorption of ultrasonic waves in air at high frequencies (10–20 MHz). *J. Acoust. Soc. Am.* **92**, 2006–2015 (1992).
45. Young, E. H. Jr & Yao, S.-K. Design considerations for acousto-optic devices. *Proc. IEEE* **69**, 54–64 (1981).
46. Maydan, D. Acoustooptical pulse modulators. *IEEE J. Quantum Electron.* **6**, 15–24 (1970).
47. Lang, T. et al. High repetition rate, low noise and wavelength stable OPCPA laser system with highly efficient broadly tunable UV conversion for FEL seeding. *EPJ Web Conferences* **267**, 01052 (2022).
48. Liu, W. & Chin, S. L. Direct measurement of the critical power of femtosecond Ti:sapphire laser pulse in air. *Opt. Express* **13**, 5750–5755 (2005).
49. Mazur, M. M. et al. Acousto-optic modulators of high-power laser radiation on the basis of KGW and KYW crystals. *Quantum Electron.* **50**, 957–961 (2020).
50. Riesbeck, T. & Lux, O. AOM fourfold pass for efficient Q-switching and stable high peak power laser pulses. *Opt. Commun.* **282**, 3789–3792 (2009).

Publisher's note Springer Nature remains neutral with regard to jurisdictional claims in published maps and institutional affiliations.

Open Access This article is licensed under a Creative Commons Attribution 4.0 International License, which permits use, sharing, adaptation, distribution and reproduction in any medium or format, as long as you give appropriate credit to the original author(s) and the source, provide a link to the Creative Commons license, and indicate if changes were made. The images or other third party material in this article are included in the article's Creative Commons license, unless indicated otherwise in a credit line to the material. If material is not included in the article's Creative Commons license and your intended use is not permitted by statutory regulation or exceeds the permitted use, you will need to obtain permission directly from the copyright holder. To view a copy of this license, visit <http://creativecommons.org/licenses/by/4.0/>.

© The Author(s) 2023

Methods

Numerical methods

We performed in-depth numerical simulations of the underlying acoustic and optic phenomena resembling the presented experimental set-up. The simulation consisted of two building blocks. The sound field is simulated using COMSOL Multiphysics. This sound field is then converted to a refractive-index field. This refractive-index field is then used as an input to the optical simulation, which is performed using the laser pulse propagation and nonlinear optics software Chi3D⁵¹. The acoustic model uses the FEM⁵² of COMSOL Multiphysics. The large ratio between the acoustic wavelength (0.7 mm) and the diameter of the reflector (75 mm) necessitates a large grid, so a 2D model is employed. The geometry considered for this model is sketched in Extended Data Fig. 1. It takes into account an ultrasound transducer implemented as an acoustic aperture with a diameter of 70 mm and, optionally, a reflector with thickness of 10 mm and diameter of 75 mm. The distance between the reflector and the ultrasound transducer is 19 mm. The sound field is generated by considering a periodic displacement of the acoustic aperture, represented by a spatially non-uniform distribution of the normal velocity of the ultrasound transducer surface. To closely match our experiment, measurements of the ultrasound transducer surface velocity in resonance are conducted using a laser-Doppler vibrometer (LDV)⁵³.

Extended Data Fig. 2a shows the 2D results of the LDV measurements without a reflector. Extended Data Fig. 2b shows the result of a line scan along the 2D transducer aperture such that it approximates the position of the modulated optical beams in our experiments inside the transducer–reflector arrangement. This 1D dataset is then used as the input to model the sound field. To resemble the experimental conditions, air at a pressure of 1,000 hPa, 21.1° C and 42.5% relative humidity is used as the material, and a perfectly matched layer (PML) is used to complete the model. This ensures absorption of all emitted waves leaving the transducer–reflector arrangement, representing an infinite propagation space for the acoustic waves. The ultrasound wave propagation simulations are based on solving the Helmholtz equation and include linear acoustic propagation and thermoviscous effects. We then convert the arising pressure field to a refractive-index modulation field Δn . Here, we consider influences arising from deviations from normal pressure ($\Delta p/p_0$) and ambient temperature ($\Delta T/T_0$) using the modified Edlén equation^{54,55}. We linearly approximate the modified Edlén equation around the ambient conditions with refractive index n as

$$\Delta n = (n - 1) \times [\Delta p/p_0 + \Delta T/T_0] \quad (3)$$

Extended Data Fig. 1b shows the emerging Δn field used in our simulations and indicates the position of the ultrasound transducer and reflector.

The optical simulations employ a split-step Fourier algorithm incorporating linear and nonlinear laser-pulse propagation effects. This includes dispersion, self-phase modulation, Kerr lensing and diffraction. This simulation considers 2 + 1 dimensions. The effect of the ultrasound pressure field is incorporated by adding a spatially dependent phase every propagation step dz , leading to an expression of the optical electric field at $z + dz$ of

$$E(\omega, y, z + dz) = E(\omega, y, z) \times \exp\{ik\Delta n(\omega, y, z) dz\} \quad (4)$$

where E is the electric field, z and y are the spatial coordinates along the optical propagation and diffraction axes, respectively, ω is the optical frequency, k is the wavevector, and $\Delta n(\omega, y, z)$ is the refractive-index modulation amplitude. In our simulation, we propagate the laser pulse seven times through the simulated sound field, reflecting the experiment. The parameters used in the simulation are listed in Extended Data Table 1.

Detection methods

Optical. We employ several detection methods for beam quality and diffraction efficiency measurements. They rely on two different approaches for separating the diffracted and transmitted beams. For efficiency and beam quality (M^2) measurements, we separate the diffracted order from the transmitted order using a D-shaped mirror placed approximately in the focal plane of a lens. Additionally, the weak higher diffraction order ($m = +2$) is removed using a knife edge. Although the energy content of the $m = +2$ beam is very low, it will still distort the beam-quality measurement. The beam-quality parameter M^2 is determined using a commercial beam profiler (Ophir-Spiricon M2-200s). The efficiency is measured by comparing the power of diffracted and transmitted orders using photodiodes after separation of the orders. This approach is verified by placing a camera in the geometrical focus of a lens and comparing the integrated pixel brightness of the $m = +1$ diffracted order to all orders. Finally, a lens telescope collimates and magnifies the output to a $1/e^2$ radius of 3.3 mm. The beam profile images, as displayed in Fig. 1d, are measured using a fibre-coupled AOM as a fast shutter spliced into the delivery fibre before entering the gas-AOM set-up to mitigate temporal averaging over multiple modulation cycles of the acoustic field. The fibre AOM gate time is set to 72 ns and is thus much shorter than the ultrasound field period ($\sim 2 \mu\text{s}$) and the camera exposure time. For the low-optical-power tests, an NKT ORIGAMI 0-10LP custom model fibre-coupled laser source is used.

The time delay between the camera exposure window and the acoustic wave can be adjusted with a delay generator (Quantum Composers Model 9514). For Fig. 1c,d and for the M^2 measurements, the delay is adjusted to the maximum diffraction efficiency, resembling measurements at the peak of the ultrasound field cycle. By adjusting the delay for the M^2 measurement, we are able to show that the beam quality is independent of the exact delay setting, and thus independent of the ultrasound amplitude. An in-depth explanation of the temporal measurement characteristics is provided in the following. For the high-optical-power experiment, an Amphos 5000 amplifier is employed. No fast shutter supporting the peak power was available. Thus, the beam profile was measured using a camera after 16.5 m of propagation with the beam path folded over multiple plane mirrors, leading to spatial separation of the transmitted and diffracted orders. Before this propagation and immediately after the AO interaction, a weak portion of the beam is sampled. After the propagation, the diffracted and transmitted orders separate and are selected using a beam aperture. The beam profiles are measured using a camera and a commercially available telescope (Thorlabs BE05-UVB). The camera, telescope and diaphragm settings and distances are identical for all three beam profiles (Fig. 3a–e), and only the final guiding mirror is tilted to select a single diffraction order.

Acoustic. For the measurements of the travelling-wave configuration, an optical microphone is used—an XARION Eta100 Ultra membrane-free optical microphone⁵⁶, specified up to 180 dB. This is placed 1 cm over the ultrasound transducer with the sensor oriented at an angle of 45° to avoid the formation of a standing wave.

Temporal characteristics

The main signals relevant for our experiment display rather complex temporal gate characteristics. The ultrasound transducer is operated in bursts so as to mitigate thermal effects and potential damage. The burst frequency is 5 Hz and the burst duration ~ 1 ms. The low-power experiment is optically gated, and the high-power laser also operates in bursts. Extended Data Fig. 3 details the temporal characteristics over these bursts for both experiments. Extended Data Fig. 3a displays the gate of the gas-based AOM applied to the AOM driver, set to a duration of 918 μs , which corresponds to 450 acoustic cycles at 490 kHz. Extended Data Fig. 3b shows the driver current, which reaches 7.5 A at a supply voltage of 16 V. The data are measured at a reduced

supply voltage to avoid saturation of the current probe. Extended Data Fig. 3c displays the time evolution of the relative powers contained in the $m = 0$ and $m = +1$ orders for both configurations, with and without the acoustic reflector. The build-up of a standing wave after the first pass of the acoustic wave is visible when the reflector is used. At approximately the fifth acoustic pass, an equilibrium is reached. The signal deteriorates slightly over time due to discharge of the capacitor banks of the AOM driver, as seen in the behaviour of the driver current. Extended Data Fig. 3d,e presents expanded views of Extended Data Fig. 3c that contain the initial build-up phase used to extract the 10–90% rise time (30 μs) as well as the steady-state signal later in the burst. The beam diameter of $2w = 6.6$ mm gives a lower bound for the rise time, which for air ($V = 343$ m s⁻¹) is 12 μs , assuming an instantaneous transducer response. The rise time is thus limited by the transducer rise time. The data agree with the transducer rise time extracted from the temporal build-up of the driver current (Extended Data Fig. 3b). Finally, Extended Data Fig. 3f displays the reconstructed burst shape of the high-power laser, displaying both the peak pulse energy and the relatively constant burst. Through the delay generator, we synchronized the gas-AOM gate to the laser burst.

Parameter regime estimation

This section explains in detail how the parameter regimes of Fig. 3f are estimated. Here, the spectral and peak power regimes in which the gas-based AOM and potentially other gas-based photonic devices may be operated are visualized in the range from below 0.1 nm (or photon energy > 10 keV) and up to 15 μm and for optical peak power ranging from -100 W to 10 TW. We display the operation regimes for the gas-phase media of ambient air (blue) and helium (yellow) and the widespread crystalline AO media quartz (purple) and TeO₂ (green), indicated using coloured areas, fading out towards unusable regimes. The displayed spectral limits are defined considering linear absorption in the medium using reported reference data: ref. 57 for ambient air, ref. 58 for helium in the extreme ultraviolet and ref. 59 elsewhere, refs. 60,61 for quartz and ref. 62 for TeO₂. In wavelength ranges where substantial absorption occurs, the colour is transparent. In the case of TeO₂, due to the lack of transmission data for wavelengths longer than 3.5 μm , this area is marked with a dotted line.

We estimate a limit for the optical peak power using the critical power, a lower bound for the power at which self-focusing and beam collapse will occur after sufficiently long propagation. The critical power for a Gaussian beam profile can be calculated as⁶³

$$P_{\text{critical}} \approx \frac{0.151\lambda^2}{n(\lambda)n_2} \quad (5)$$

The critical power depends on the optical wavelength λ , the wavelength-dependent refractive index $n(\lambda)$ and the nonlinear refractive index n_2 . This value is independent of beam size, so the applicable range may be extended beyond the critical power by limiting the propagation length in the medium and increasing the beam size. For this reason, we choose the critical power as a reference for the limit, but fade the colour out in the range $[P_{\text{critical}}; 10P_{\text{critical}}]$.

The used wavelength-dependent refractive indices are taken from ref. 64 for air, refs. 65,66 for helium, refs. 67,68 for quartz and ref. 69 for TeO₂. For helium, for $\lambda > 1$ μm we assume n to be constant due to the lack of reference data. The nonlinear indices were assumed to be constant over the displayed wavelength range, and taken from ref. 70 for air, ref. 71 for helium, ref. 72 for quartz and ref. 62 for TeO₂. This assumption is not justifiable at very high photon energies where a nonlinear index is not available. This corresponding parameter region therefore does not display a clear peak power bound, as indicated by the dotted markers.

Data availability

All data and materials used in the analysis are available in the text, Methods, Extended Data or from the authors upon reasonable request.

Code availability

All code used in the analysis is available from the authors upon reasonable request.

References

- Lang, T. et al. Impact of temporal, spatial and cascaded effects on the pulse formation in ultra-broadband parametric amplifiers. *Opt. Express* **21**, 949–959 (2013).
- Turner, M. J. et al. Stiffness and deflection analysis of complex structures. *J. Aero. Sci.* **23**, 805–823 (1956).
- Rothberg, S. J. et al. An international review of laser Doppler vibrometry: making light work of vibration measurement. *Opt. Lasers Eng.* **99**, 11–22 (2017).
- Edlén, B. The refractive index of air. *Metrologia* **2**, 71–80 (1966).
- Birch, K. P. & Downs, M. J. Correction to the updated Edlén equation for the refractive index of air. *Metrologia* **31**, 315–316 (1994).
- Fischer, B. Optical microphone hears ultrasound. *Nature Photon.* **10**, 356–358 (2016).
- Naval Air Warfare Center. in *Electronic Warfare and Radar Systems Engineering Handbook* 4th edn, 7–1.17 (Technical Communication Office, NAWCWD, 2013).
- Henke, B. L., Gullikson, E. M. & Davis, J. C. X-ray interactions: photoabsorption, scattering, transmission and reflection at $E = 50$ –30,000 eV, $Z = 1$ –92. *Atom. Data Nuclear Data Tables* **54**, 181–342 (1993).
- Sansonetti, J. E. & Martin, W. C. Handbook of basic atomic spectroscopic data. *J. Phys. Chem. Ref. Data* **34**, 1559–2259 (2005).
- Saito, K. & Ikushima, A. J. Absorption edge in silica glass. *Phys. Rev. B* **62**, 8584–8587 (2000).
- Linstrom, P. *NIST Chemistry WebBook, NIST Standard Reference Database* 69 (NIST, 1997).
- Kim, S.-H., Yoko, T. & Sakka, S. Linear and nonlinear optical properties of TeO₂ glass. *J. Am. Ceramic Soc.* **76**, 2486–2490 (1993).
- Fibich, G. & Gaeta, A. L. Critical power for self-focusing in bulk media and in hollow waveguides. *Opt. Lett.* **25**, 335–337 (2000).
- Peck, E. R. & Reeder, K. Dispersion of air. *J. Opt. Soc. Am.* **62**, 958–962 (1972).
- Huber, M. C. E. & Tondello, G. Refractive index of He in the region 920–1,910 Å. *J. Opt. Soc. Am.* **64**, 390–392 (1974).
- Ermolov, A. et al. Supercontinuum generation in the vacuum ultraviolet through dispersive-wave and soliton-plasma interaction in a noble-gas-filled hollow-core photonic crystal fiber. *Phys. Rev. A* **92**, 033821 (2015).
- Malitson, I. H. Interspecimen comparison of the refractive index of fused silica. *J. Opt. Soc. Am.* **55**, 1205–1209 (1965).
- Tan, C. Z. Determination of refractive index of silica glass for infrared wavelengths by IR spectroscopy. *J. Non-Cryst. Solids* **223**, 158–163 (1998).
- Uchida, N. Optical properties of single-crystal paratellurite (TeO₂). *Phys. Rev. B* **4**, 3736–3745 (1971).
- Nibbering, E. T. J. et al. Determination of the inertial contribution to the nonlinear refractive index of air, N₂ and O₂ by use of unfocused high-intensity femtosecond laser pulses. *J. Opt. Soc. Am. B* **14**, 650–660 (1997).
- Bree, C., Demircan, A. & Steinmeyer, G. Method for computing the nonlinear refractive index via Keldysh theory. *IEEE J. Quantum Electron.* **46**, 433–437 (2010).
- Milam, D. Review and assessment of measured values of the nonlinear refractive-index coefficient of fused silica. *Appl. Opt.* **37**, 546–550 (1998).

Acknowledgements

We acknowledge Deutsches Elektronen-Synchrotron DESY (Hamburg, Germany), the Helmholtz Institute Jena (Jena, Germany) and members

of the Helmholtz Association HGF for support and/or the provision of experimental facilities. We disclose support for the research of this work from Deutsches Elektronen-Synchrotron DESY, the DESY Generator Program and Klaus Tschira Foundation, the Klaus Tschira Boost Fund (GSO/KT 29; C.M.H.), the Carl Zeiss Foundation, CZS Wildcard (P2022-03-018; A.H., M. Kupnik and C.M.H.) and from a Seventh Framework Programme (FP7) FP7/2007-2013 European Research Council (ERC) Synergy Grant (609920; F.X.K.).

Author contributions

Conceptualization was provided by Y.S., C.H., T.L., T.H.-J., M. Kupnik and C.M.H. The methodology was designed by Y.S., C.H., T.L., M.R., T.H.-J., S.S., A.H., I.H., M. Kupnik and C.M.H. The software was written and designed by Y.S., C.H., T.L. and M.R. Formal analysis was performed by Y.S., C.H., T.L. and M.R. Investigation was carried out by Y.S., C.H., T.L., J.Z., M.S., M.R., S.H.S., S.S., M. Kellert and J.H.D. Resources were supplied, acquired and managed by T.L., J.Z., M.P., T.H.-J., F.X.K., I.H., M. Kupnik and C.M.H. Data curation was performed by Y.S. and C.H. The original draft for this paper was written by Y.S. and C.M.H., and review and editing was performed by Y.S., T.L., C.M.H. and all other co-authors. Visualization was carried out by Y.S. Supervision was performed by A.H., W.P.L., I.H., M. Kupnik and C.M.H. The project was administered by C.M.H. Funding was acquired by A.H., M. Kupnik and C.M.H.

Competing interests

T.H.-J. is CEO of inoson GmbH (St. Ingbert). C.M.H. and T.L. have co-filed a (pending) patent on 27 October 2020

entitled ‘Acousto-optical modulator apparatus and method of acousto-optically deflecting a laser beam’, published as EP3992707A1 and US2022128883A1. Applicants for this patent are Deutsches Elektronen-Synchrotron DESY and GSI Helmholtzzentrum für Schwerionenforschung GmbH, and the inventors are Christoph Heyl and Tino Lang. This patent involves an acousto-optical modulator apparatus for acousto-optically deflecting a laser beam and comprises a gas-filled volume including a working gas. All other authors declare no competing interests.

Additional information

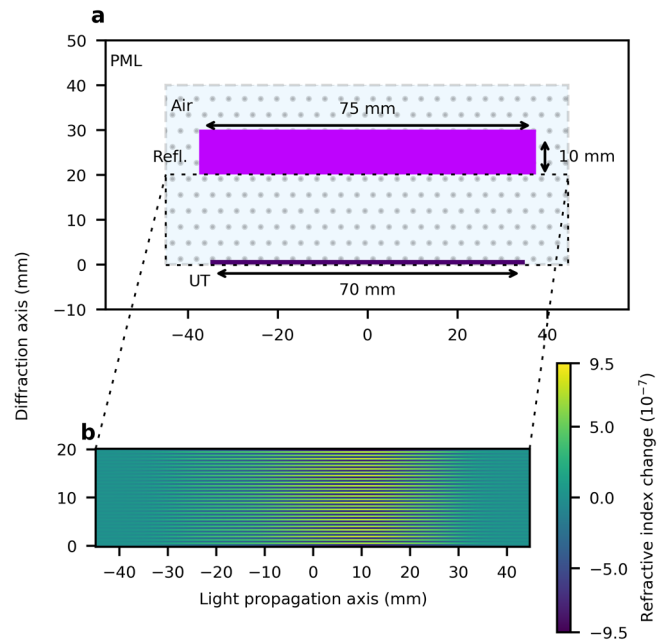
Extended data is available for this paper at <https://doi.org/10.1038/s41566-023-01304-y>.

Supplementary information The online version contains supplementary material available at <https://doi.org/10.1038/s41566-023-01304-y>.

Correspondence and requests for materials should be addressed to Yannick Schrödel or Christoph M. Heyl.

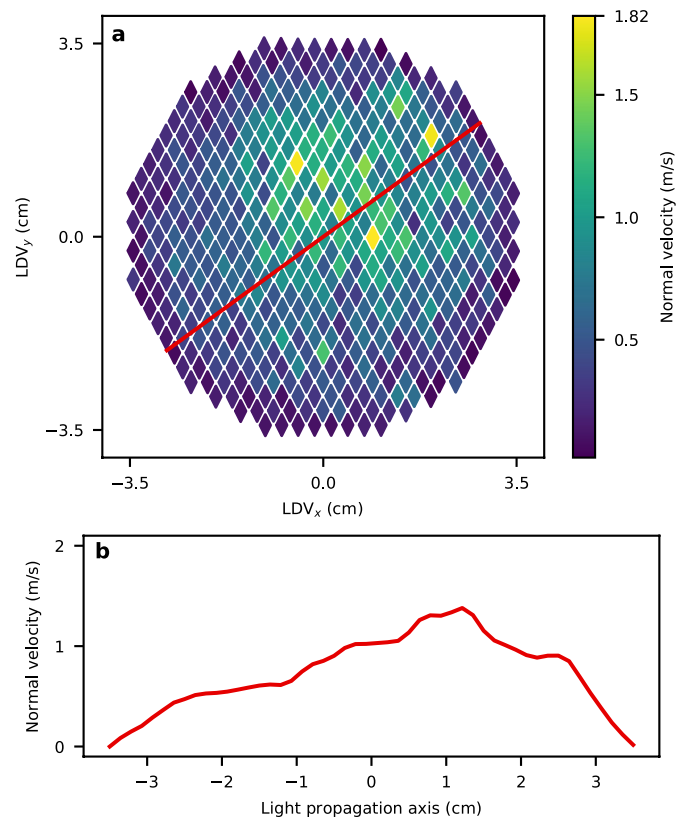
Peer review information *Nature Photonics* thanks Günter Steinmeyer, Robert Bingham and the other, anonymous, reviewer(s) for their contribution to the peer review of this work.

Reprints and permissions information is available at www.nature.com/reprints.

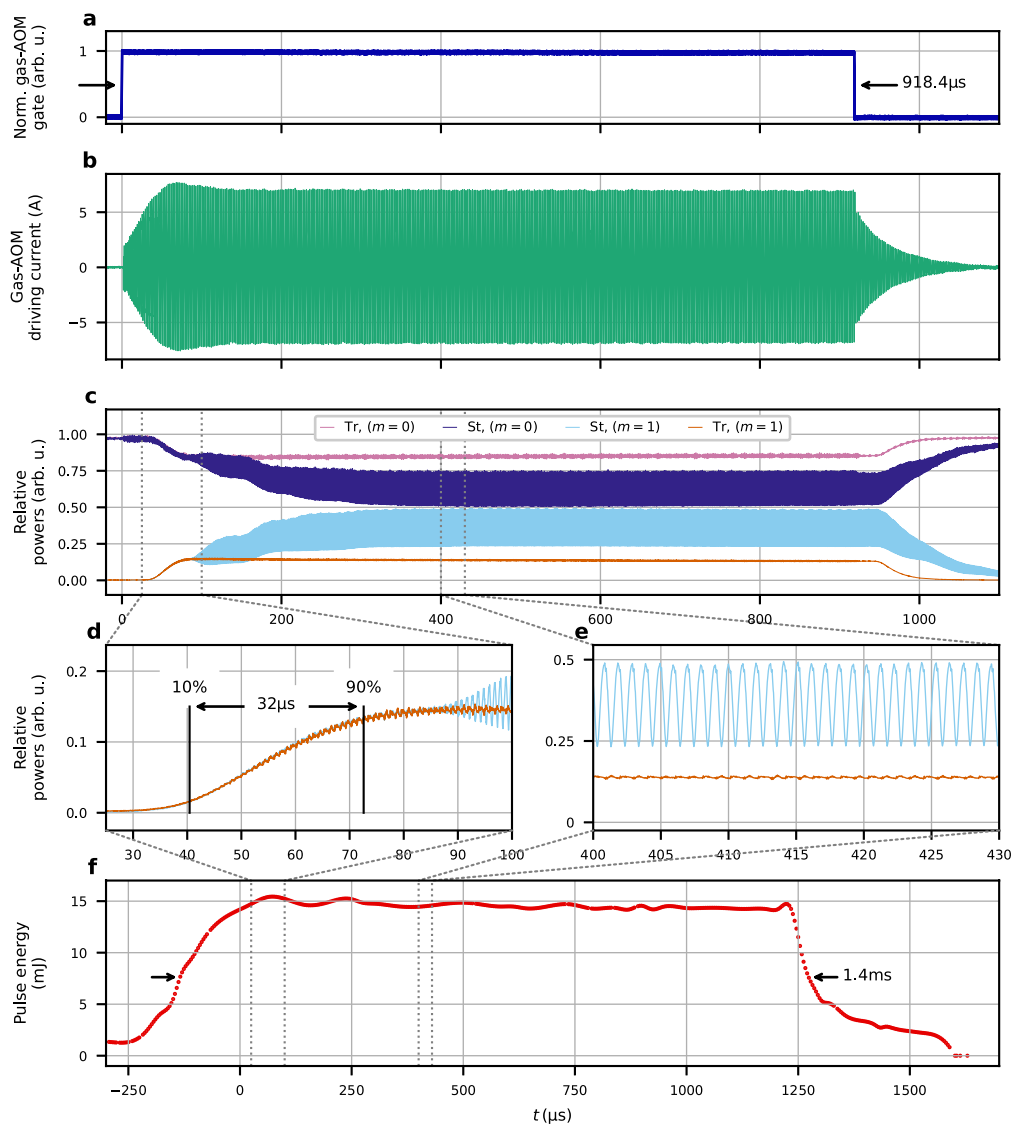


Extended Data Fig. 1 | Schematic of the geometry used for the acoustic simulation. **a**, A perfectly matched layer (PML) surrounds the air-filled region. UT is the ultrasound transducer with an active area which exhibits a normal surface velocity distribution characterized using LDV measurements (see

Extended Data Fig. 2). The optional reflector is indicated (Refl., purple area). **b**, The resulting refractive index modulation obtained from the COMSOL model and the LDV measurements.



Extended Data Fig. 2 | Raw data of the LDV measurements of the employed ultrasound transducer. a, Spatial distribution of the normal surface velocity of the ultrasound transducer. The red line indicates the approximate line-out location used for the 2D acoustic simulation. **b**, The extracted one-dimensional surface velocity along the red line displayed in a.



Extended Data Fig. 3 | Temporal characteristics of key parameters used for the reported experiments. **a**, Gate for the gas-AOM driver. **b**, Gas-AOM driver current. **c–e**, Relative powers of diffracted ($m = +1$) and transmitted ($m = 0$) orders of both standing (St., light/dark blue lines) and travelling (Tr., orange/

purple lines) wave configurations. **f**, The reconstructed optical burst shape of the gigawatt-scale laser system. Red dots indicate individual pulses used for the pulse energy calculations.

Extended Data Table 1 | Simulation inputs

Simulation parameter	
Optical	
$1/e^2$ beam radius	3.25 mm
Optical wavelength	1030 nm
Pulse duration	500 fs
Pulse energy	10 mJ
Number of passes over sound field	7
Acoustic	
AO interaction length per pass	70 mm
Free space propagation per pass	80 mm
Ambient temperature	21.1 °C
Relative humidity	42.5%
Acoustic frequency	490 kHz

Parameters used for the numerical simulations of the gas-phase acousto-optic interaction.